ADVANCED ENERGY MATERIALS
www.advenergymat.de

On the Interplay between CT and Singlet Exciton Emission in Organic Solar Cells with Small Driving Force and Its Impact on Voltage Loss

*Tobias Fritsch, Jona Kurpiers, Steffen Roland, Nurlan Tokmoldin, Safa Shoaee, Thomas Ferron, Brian A. Collins, Silvia Janietz, Koen Vandewal, and Dieter Neher**

The interplay between free charge carriers, charge transfer (CT) states and singlet excitons (S_1) determines the recombination pathway and the resulting open circuit voltage (V_{OC}) of organic solar cells. By combining a well-aggregated low bandgap polymer with different blend ratios of the fullerenes PCBM and ICBA, the energy of the CT state (E_{CT}) is varied by 130 meV while leaving the S_1 energy of the polymer (E_{S_1}) unaffected. It is found that the polymer exciton dominates the radiative properties of the blend when E_{CT} approaches E_{S_1}, while the V_{OC} remains limited by the non-radiative decay of the CT state. It is concluded that an increasing strength of the exciton in the optical spectra of organic solar cells will generally decrease the non-radiative voltage loss because it lowers the radiative V_{OC} limit ($V_{OC,rad}$), but not because it is more emissive. The analysis further suggests that electronic coupling between the CT state and the S_1 will not improve the V_{OC}, but rather reduce the $V_{OC,rad}$. It is anticipated that only at very low CT state absorption combined with a fairly high CT radiative efficiency the solar cell benefit from the radiative properties of the singlet excitons.

1. Introduction

Since the first NREL certification in 2001, the power conversion efficiency of organic photovoltaics (OPV) has greatly increased from 2.5%[1] up to over 19% for single junction and 20% for tandem devices.[2,3] Understanding free charge recombination and the associated open circuit voltage (V_{OC}) loss is amongst the most important issues to push the efficiency of these devices toward and over 20%.[4] It is generally accepted that free charge carrier recombination proceeds primarily via reformation and decay of charge transfer (CT) states, involving radiative and non-radiative pathways. The latter typically dominates the decay rate and is, therefore, mainly responsible for the V_{OC} loss. It was further shown that non-radiative decay is dominated by vibronic coupling and that it is dependent on the CT state energy via an energy gap law.[5,6] The situation becomes more complex when the energy of the CT state, approaches the energy of the lowest singlet exciton, the local exciton of the component dominating the optical gap. In this case, reformation of the singlet exciton from the CT state becomes more likely, documented, for example, by an increased singlet exciton emission intensity in electroluminescence (EL).[7,8] Recent experimental and theoretical work suggested that the singlet excitons and CT states are in dynamic equilibrium, meaning that the populations of the two excited species are coupled.[9–11] For a very small difference between the CT and the lowest singlet exciton, ΔE_{S_1-CT}, often denoted as the driving force for charge generation, the charge recombination pathway becomes influenced by the S_1 properties.[12,13] As singlet excitons are generally more emissive than CT states, this causes a significant reduction of the non-radiative voltage loss, which depends logarithmically on the ratio between the non-radiative and the radiative decay rates. However, predominant emission from the S_1 state does not imply that all free charge recombination proceeds through this channel. This is due to the fact that recombination still occurs through the CT state and that its decay is highly non-radiative. For the prototypical PM6:Y6 blend, we have recently shown that more than 90% of the radiative decay occurs through the singlet exciton, but that the total recombination current is almost entirely determined by the non-radiative decay of the CT state,

T. Fritsch, J. Kurpiers, S. Roland, N. Tokmoldin, S. Shoaee, D. Neher
Institute of Physics and Astronomy
University of Potsdam
14476 Potsdam, Germany
E-mail: neher@uni-potsdam.de
T. Fritsch
Department 8.5 Micro-NDT
Federal Institute of Materials Research and Testing
Unter den Eichen 87, 12205 Berlin, Germany
T. Ferron, B. A. Collins
Department of Physics and Astronomy
Washington State University
100 Dairy Road, Pullman, WA 99164, USA
S. Janietz
Polymers and Electronics
Fraunhofer Institute for Applied Polymer Research
Geiselbergstr. 69, 14476 Potsdam, Germany
K. Vandewal
Institute for Materials Research (IMO-IMOMEC)
Hasselt University
Wetenschapspark 1, Diepenbeek BE – 3590, Belgium

The ORCID identification number(s) for the author(s) of this article can be found under https://doi.org/10.1002/aenm.202200641.

DOI: 10.1002/aenm.202200641

and thus the reason for the fairly large non-radiative voltage loss ($\Delta V_{OC,nrad}$) in this blend.[10] Understanding the interplay between these two states and how they determine the voltage losses in relation to ΔE_{S_1-CT} is therefore of great interest.

In most of the recent studies, ΔE_{S_1-CT} was varied by exchanging both the low and the high bandgap components of the donor–acceptor (D:A) blend. Changes of the morphology within such series of blends are, therefore, likely. More importantly, the absorption and emission properties of the low energy component, which are most relevant for understanding the role of the local excitons on the V_{OC} losses, often vary as well. Here, we take a different approach. We choose a well-aggregated conjugated donor polymer as the low energy component, ensuring the same S_1 properties for all blends, while the CT energy is varied through the compositional tuning of a binary fullerene-based acceptor phase. By decomposing the EL and photovoltaic external quantum efficiency (EQE_{PV}) spectra into the singlet and CT components, we quantify the contributions of these two states to photon absorption and emission. The analysis shows that the emission of the ternary blends becomes dominated by the polymer S_1 for high E_{CT}, and that the radiative upper limit for V_{OC} quickly approaches a constant value determined by the singlet energy of the low band gap component (in this case the polymer). By analyzing all other contributions to the recombination current, we show that the non-radiative decay of the CT state determines V_{OC} for all ΔE_{S_1-CT}. In turn, the non-radiative V_{OC} loss is independent of the emission properties of S_1. Our work shows that a strong singlet exciton contribution in the absorption and emission does not necessarily imply that the singlet state properties affect the V_{OC} and that a detailed knowledge about the CT state and its interplay with S_1 is needed to draw firm conclusions about the origin of the voltage loss.

2. Results

2.1. Structural and Optical Properties of the Blend

Our ternary donor–acceptor bulk heterojunction (BHJ) system comprises the fluorinated donor copolymer poly[2,6-(4,4-bis(2-ethylhexyl)-4H-cyclopenta[2,1-b;3,4-b′]dithiophene)-*alt*-4,7-(2,1,3-benzothiadiazole)] (1F-PCPDTBT), and the two fullerene acceptors PCBM and ICBA (see **Figure 1**a for the chemical structures and the energy levels). The mixture of PCBM of ICBA has been studied in great detail in the past, where it was shown that the V_{OC} of such mixture with a donor polymer can be tuned in small steps.[14–16] 1F-PCPDTBT has been chosen for several reasons. First, it forms well-performing blends with PCBM. Second, its absorption and emission are well-separated from that of PCBM and ICBA.[17] Third, it aggregates strongly in thin films of neat material as well

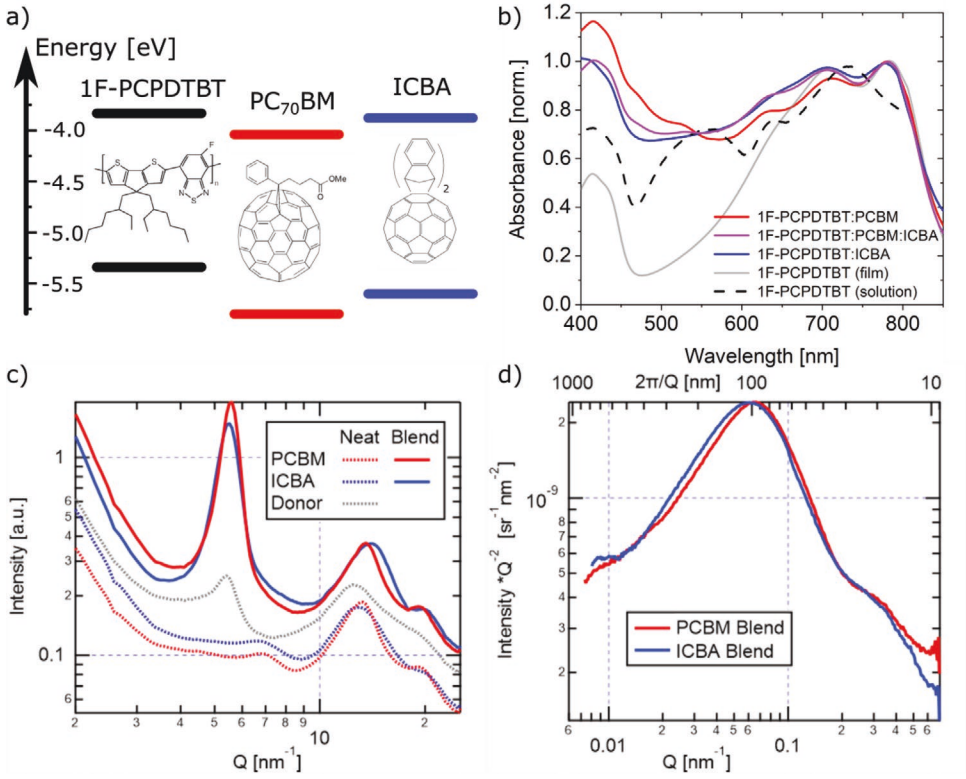

Figure 1. a) Chemical structure and energy diagram of the donor polymer and the two fullerenes. b) Normalized absorption spectra of films of a neat 1F-PCPDTBT film (grey) compared to the blends with PCBM (red), ICBA (blue), and a PCBM:ICBA 1:1 mixture (pink). The long wavelength region of the blend beyond 700 nm is entirely dominated by the donor polymer. Also shown is the absorption of the polymer in solution (black, dashed). c) GIWAXS scattering profiles in the out-of-plane direction for both blends and neat films of the components. Scattering of the neat components are offset vertically for clarity. d) Lorentz corrected RSoXS profiles for both blends acquired with a photon energy of 283.5 eV, which is just below the fullerene absorption peak to enhance phase contrast but limit absorption damage.

as in blends with fullerenes.[18] As shown in Figure 1b, the shape and spectral position of the low energy absorption in the blend is the same as that of the neat polymer film, and very different from that of the non-aggregated polymer in solution.

To investigate in detail how the choice of the fullerene affects the polymer crystallinity, 1F-PCPDTBT:ICBA was studied in comparison to 1F-PCPCTBT:PCBM through grazing incident wide angle X-ray scattering (GIWAXS) and resonant soft X-ray scattering (RSoXS). The structural data of the 1F-PCPDTBT:PCBM blend have been published before.[19] Figure 1c shows the 1D GIWAXS profiles in the out-of-plane direction in the film for the neat components to aid peak identification. 1F-PCPDTBT has a strong (100) peak at $q = 5.5$ nm^{-1}, and retains a similar intensity even when paired with either fullerene, indicating polymer aggregation into pure crystallites. Similarly, scattering peaks at $q = 15$ nm^{-1} indicate the presence of fullerene aggregation in each film. The crystalline coherence length (CCL) for fullerene aggregates is calculated in each blend from peak fits, yielding values of 1.78(2) and 1.42(2) nm for PCBM and ICBA blends, respectively. This indicates a better aggregation of PCBM compared to ICBA. These coherence lengths are nearly identical to those of pure PCBM and ICBA, indicating pure fullerene domains form within the blends.

The mesoscale compositional domain structure was studied with RSoXS and Figure 1d displays Lorentz corrected RSoXS profiles near the carbon absorption edge. The profiles reveal a distinct blend domain structure with the primary feature at $q \approx 0.06$ nm^{-1} corresponding to a characteristic length scale of ≈100 nm. The presence of a secondary feature at $q \approx 0.3$ nm^{-1} is likely due to a scattering form factor resulting from polymer fibrils. The nearly perfect overlap of red and blue RSoXS profiles in Figure 1d indicates essentially identical domain structure within each fullerene blend. Just as the intensities of the two profiles are identical, so is the total scattering intensity, which is proportional to the mean squared differences in domain composition.[20] Combining GIWAXS and RSoXS results, it is clear that the polymer and fullerene both form pure domains within this blend, and that the domain size is unaffected by the choice of the fullerenes studied here.

2.2. Photovoltaic Device Properties

All blends were processed in solution of 1,2-dichlorobenzene, to which diiodooctane (DIO) was added at 1% as an additive to improve the performance of the processed cells (see the Supporting Information for details of the thin film and device preparation).[18,21,22] The polymer:fullerene mass-ratio was kept constant at 1:3, with an ICBA content x as defined by 1F-PCPDTBT:PC$_{70}$BM:ICBA $1 : 3(1–x) : 3x$, with x being varied from 0 to 1. Note that the blends were prepared in two series, first with $x = 0$, 0.33, 0.5, 1.0 and later with $x = 0.2$, 0.75, 0.8, and 0.9 "to fill the gaps." Because of unavoidable differences in the preparation conditions (temperature of the glove box, exact solution concentration), the results from the two series vary slightly in detail, which, however, does not affect the general conclusions from this work.

The J–V-characteristics of the solar cells with different blend ratios are shown in **Figure 2**a and the photovoltaic parameters are listed in Table S1, Supporting Information. The V_{OC} increases continuously by nearly 0.2 V, from 0.74 to 0.92 V with increasing the ICBA content, while J_{SC} and FF decrease at the same time. As shown earlier, ICBA domains exhibit a smaller CCL. Several studies have highlighted how the inability of ICBA to form well-aggregated domains renders charge formation and extraction less efficient than in the comparable PCBM-rich blends.[23–25] The corresponding photovoltaic external quantum efficiency (EQE_{PV}) spectra (Figure 2b), plotted on a logarithmic scale in the absorption tail region, and normalized to emphasize the spectral changes in the CT absorption range, exhibit a broad low energy shoulder below the bandgap of the polymer at 1.51 eV (see Figure S1, Supporting Information, for the EQE_{PV} spectra over a wider spectral range). The shoulder is most pronounced and clearly Gaussian-shaped for $x = 0$ and $x = 0.2$. The tail becomes narrower and steeper with increasing ICBA concentration, assigned to a continuous increase of E_{CT}. The EL spectra in Figure 2c are composed of a sharp peak with constant energy of 1.47 eV, which is the 0–0 transition of the polymer singlet exciton, and a broad low energy peak which moves to higher energies with increasing ICBA concentration, assigned to CT state emission. At the same time, the external quantum efficiency of EL, ELQY, increases by two orders of magnitude (see Table S1, Supporting Information). We interpret this as an increased population of the polymer S_1 as ΔE_{S_1-CT} becomes smaller.[9,12]

According to Rau,[26] the V_{OC} is equal to the radiative limit of the open-circuit voltage ($V_{OC,rad}$) minus the non-radiative voltage loss ($\Delta V_{OC,nrad}$):

$$V_{OC} = V_{OC,rad} - \Delta V_{OC,nrad} = \frac{k_B T}{q} \ln\left(\frac{J_R}{J^0_{rad}}\right) + \frac{k_B T}{q} \ln(\mathrm{ELQY}) \quad (1)$$

Here, k_B is the Boltzmann constant, T the temperature, and q the elementary charge. J_R is the current density of free charge recombination under 1 sun illumination at V_{OC} condition. It is common to assume that J_R is equal to J_{SC} as we do in this work. This assumption is not strictly correct, for example, in case of a pronounced field dependence of generation. On the other hand, J_R enters Equation (1) only in the argument of the natural logarithm. Therefore, even a factor 3 difference between J_R and J_{SC} has no profound effect on the V_{OC}. Likewise, $J^0_{Rad} = q \int_0^\infty \mathrm{EQE}_{PV}(\hbar\omega) \Phi_{BB}(\hbar\omega) d\hbar\omega$ is the radiative dark recombination current where Φ_{BB} is the black body radiation flux at room temperature. As shown in Figure 2d, the experimental V_{OC} is very well reproduced by Equation (1), where ELQY was measured and J^0_{Rad} calculated from the $EQE_{PV}(\hbar\omega)$ spectra, extended to low photon energies by applying Rau's reciprocity to the EL spectra.[26] Notably, while $V_{OC,rad}$ increases only moderately with x, the rise of the measured V_{OC} is more pronounced, especially above $x \cong 0.7$. As a consequence, $\Delta V_{OC,nrad}$ decreases to 0.25 V; a very low value for fullerene-based OPV blends.[12] However, a low $\Delta V_{OC,nrad}$ is only beneficial for the overall V_{OC} if at the same time $V_{OC,rad}$ remains high. This raises the question of the role of the polymer singlet state and its radiative decay in the charge recombination process.

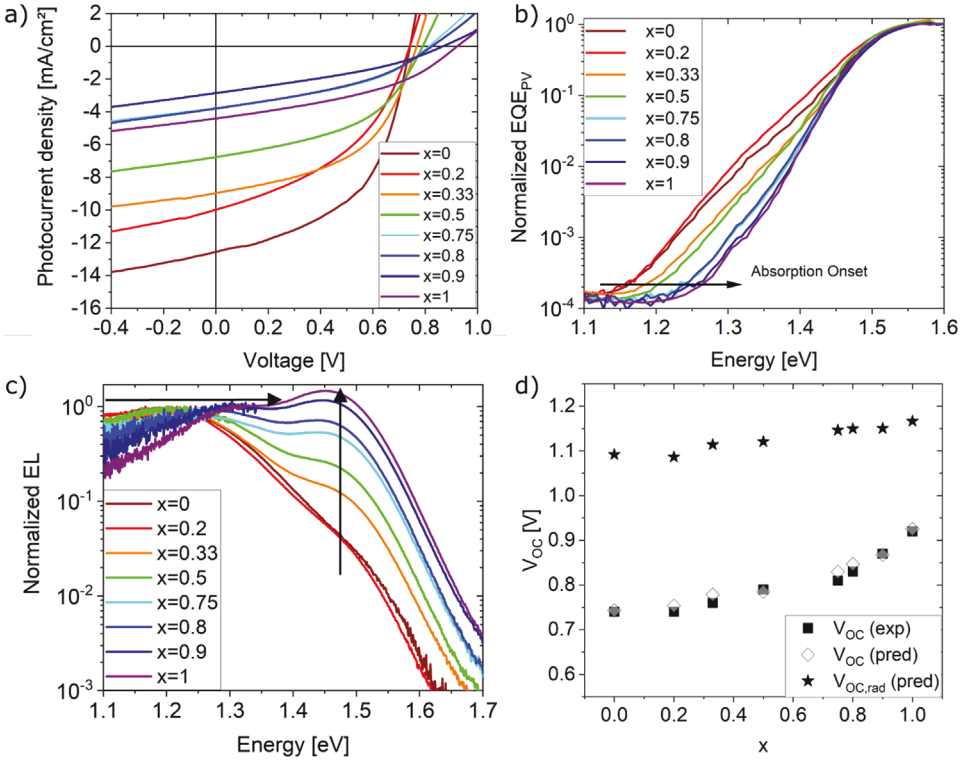

Figure 2. a) *J*–*V*-characteristics under simulated 1 sun illumination for different PCBM:ICBA mixtures. Here, x is the ICBA content with regard to PCBM. b) EQE_{PV} spectra off all blends, normalized at the maximum of the polymer singlet absorption. c) EL-spectra of the blends normalized at the CT-emission region (see below). d) V_{OC} versus the ICBA fraction. The experimental values (solid squares) are well reproduced by Equation (1) (open diamonds). Also shown is the predicted radiative V_{OC} (stars).

2.3. Spectral Deconvolution and CT Energy

The fact that the low bandgap component is a well-aggregated polymer whose properties barely change with blend composition allows us to deconvolute the EL spectra into the S_1 and CT components and to determine the CT energy for all x values. To deconvolute the spectra, it is common to measure the EL of a device of the neat low bandgap component and to subtract it from the full spectrum. However, as compared to the neat polymer films, the blend has a lower polymer content, altering the degree of reabsorption. Also, the different refractive indices of the neat and blend layers may alter the shape of the absorption and emission spectra through microcavity effects.[27,28] We therefore applied a two-step procedure: First, the S_1 EL spectrum was measured on a device of neat 1F-PCPDTBT and subtracted from the EL spectrum of the $x = 0.5$ blend. This composition was chosen because it exhibits well-pronounced CT and S_1 contributions in EQE_{PV} and EL. The remaining signal exhibits a nearly Gaussian-type line shape, which we assign to emission from the CT state. This spectrum was fitted, together with the low energy tail of the EQE_{PV} spectra according to

$$EQE_{PV}(E) = \frac{f_{EQE}}{E\sqrt{4\pi\lambda k_B T}} \exp\left(\frac{-(E_{CT}+\lambda-E)^2}{4\lambda k_B T}\right) \quad (2)$$

$$I_{EL}(E) = \frac{f_{EL}E}{\sqrt{4\pi\lambda k_B T}} \exp\left(\frac{-(E_{CT}-\lambda-E)^2}{4\lambda k_B T}\right) \quad (3)$$

Here, E is the photon energy, E_{CT} energy of the CT state, λ is the reorganization energy, and f_{EQE} and f_{EL} are pre-factors. Then, the Gaussian emission from the best fit was subtracted from the total emission spectrum to obtain the singlet emission component of the polymer in the actual blend (**Figure 3**a). When we now subtracted this specific polymer reference spectrum from the $I_{EL}(E)$ of the other blend compositions, the remaining part was always Gaussian-shaped (Figure S2, Supporting Information), allowing for a precise determination of the CT energy for different x values (note that the $x = 1$ spectrum revealed a slight modulation at the high energy side reminding of the S_1 vibrational progression, but a Gaussian-fit to the lower energy part is still meaningful). Details about the fitting procedure and the resulting parameters can be found in the Supporting Information and in Table S1, Supporting Information. With increasing ICBA content, E_{CT} increases continuously from 1.35 to 1.48 eV, approaching the energy of the polymer singlet exciton of 1.51 eV (as determined by the intersection of the absorption and emission spectra of a neat polymer film).

Before turning to the interpretation of the spectral contributions, we revisit the recent literature on the energetics of fullerene blends. Street and coworkers proposed that electrons delocalize over both kinds of fullerenes resulting in one alloy CT-state, whose energy depends on composition.[14] Other papers suggested that the nature and energy of the two types of donor–acceptor pairs in the ternary blend is

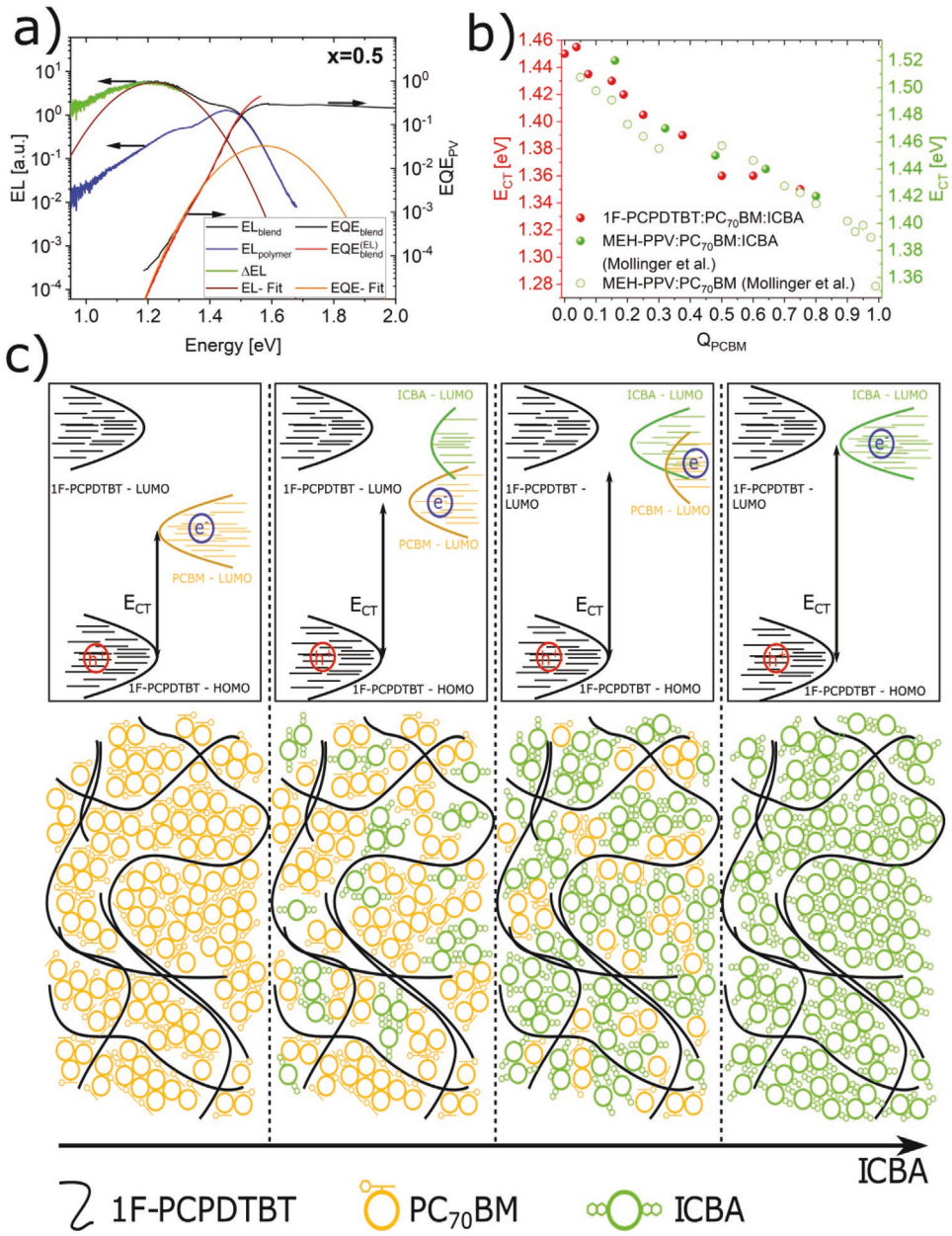

Figure 3. a) Experimental EL and EQE_{PV} spectra for the example of $x = 0.5$, together with the Gaussian fits to the CT absorption and emission. b) The estimated CT-energy of the ternary blends as a function of the fraction of nearest PCBM neighbors Q_{PCBM} (red circles), together with the corresponding values of Mollinger et al. (green circles). c) Schematic explanation for the increase of E_{CT} with increasing ICBA content. The presence of the ICBA molecules in the blend reduces the PCBM aggregation, going along with an upshift of the PCBM-LUMO and the related CT state energy. Its only for high ICBA concentration that the CT properties are becoming dominated by the ICBA-polymer heterojunction.

the same as in the corresponding binary blends, meaning that the density of states distribution of the ternary system is the composition-weighted sum of the state manifolds of the two binaries.[15,29,30] As documented in Figure S3a, Supporting Information, the characteristic changes in our EQE_{PV} spectra are neither consistent with the superposition model nor can they be explained by assuming the formation of an alloy. Recent work shows strong evidence for a pronounced effect of the blend composition on the energy and spectral width of the individual CT states, either through aggregation or micro electrostatics.[28,29] For PCBM, the electron affinity decreased by 100–200 meV upon deaggregation,[23,31] comparable to the LUMO difference of neat PCBM and ICBA. In contrast, ICBA does not form crystalline domains and its optical and electronic properties are barely affected by dilution.[31] Based on this, Mollinger developed a picture to explain the dependence of E_{CT} on the ICBA concentration in blend of the donor polymer MEH-PPV with a PCBM:ICBA mixture.[29] Here, replacing PCBM by ICBA reduces the PCBM aggregate size, therefore raising its LUMO level and consequently

E_{CT}. To rule out a pronounced hybridization or alloying of the two kinds of fullerenes on E_{CT}, the authors studied a binary MEH-PPV:PCBM blend with varying polymer:fullerene ratio. In Figure 3b we plotted E_{CT} of their binary and ternary blends (green full and empty circles) as a function of Q_{PCBM}. Here, Q_{PCBM} is the probability that the neighbor of a PCBM molecule is also PCBM. Both cases display the very same steady increase of E_{CT} with increasing ICBA-content (smaller Q_{PCBM}) over a range of 100 meV. Despite the choice of a rather different donor polymer, our blends follow the very same trend, with a shift in the absolute CT energy which is due to the different ionization energy of 1F-PCPDTBT. This allows us to draw the following picture of the energetics and state occupation in our 1F-PCPDTBT:PCBM:ICBA ternary blends (Figure 3c): for low to intermediate x, the CT manifold is entirely dominated by the polymer:PCBM interface. Increasing x decreases the size of the PCBM aggregates and increases the mean energy of the 1F-PCPDTBT:PCBM CT state. This energy finally approaches that of the 1F-PCPDTBT:ICBA interface for large x, which finally becomes the CT state dominating absorption and emission. As such, it is meaningful to describe the interfacial energetics by one CT state, which increases continuously with Q_{PCBM}, without an abrupt transition.

We note here that all of these states are broadened by dynamic and static energetic disorder.[32,33] We have not taken disorder into account in our models, as we are mainly interested in the interplay between CT and S_1 state emission. Disorder is an important parameter when aiming at predicting the V_{OC} for a given CT energetics and decay rate.[30,34] Part of the spectral shift of the EL emission may actually origin from the fact that decreasing the PCBM concentration reduces the number density of polymer:PCBM CT states, which for a given recombination current and CT decay rate causes state filling of the energetically broadened DOS. This in turn increases the value of E_{CT} as deduced from the spectra and finally the V_{OC} (e.g., decreasing the CT number density by a factor of ten raises V_{OC} by ca 56 mV at room temperature).[34] Fortunately, the conclusions from our analysis (Equations (4)–(7)) are independent of the actual width of the distributions and the actual mechanisms causing the rise of E_{CT} with decreasing PCBM concentration. The reason is that E_{CT} does not enter the relevant equations directly but is rather used to estimate ΔE_{S_1-CT} as a measure of the energetic offset between the (occupied) S_1 and CT state manifolds.

2.4. Singlet Emission and Non-Radiative Voltage Loss

As pointed out earlier, it has been suggested that for a small ΔE_{S_1-CT} the population of the emissive singlet exciton states decreases the non-radiative voltage loss through an increase of the ELQY. Indeed, the EL spectrum of our blends becomes dominated by the singlet emission component for high x, while at the same time $\Delta V_{OC,nrad}$ reduces to 250 meV. On the other hand, it was argued that a strong singlet emission does not necessary improve the V_{OC}.[10] This is the case when recombination proceeds almost entirely through the CT state, rendering emissive decay of the much less populated singlet state irrelevant for the V_{OC}.

It can be generally assumed that the exciton and CT state population are in dynamic equilibrium.[10,11,35] Then, the following equations can be derived (see the Supporting Information for the derivation)

$$qV_{OC} = \mu = k_B T \ln\left\{\frac{J_R}{\frac{J^0_{rad,CT}}{ERE_{CT}} + \frac{J^0_{rad,S_1}}{ERE_{S_1}}}\right\} \quad (4)$$

$$qV_{OC,rad} = \mu_{rad} = k_B T \ln\left\{\frac{J_R}{J^0_{rad,CT} + J^0_{rad,S_1}}\right\} \quad (5)$$

Here, $\mu = \mu_{CT} = \mu_{S_1}$ is the global chemical potential of the illuminated blend, which in absence of bending of the quasi-Fermi levels is equal to qV_{OC}. μ_{rad} is the chemical potential if all recombinations were radiative. $J^0_{rad,CT}$ and J^0_{rad,S_1} is the dark recombination current of the CT and S_1 state, respectively. ERE_{CT} and ERE_{S_1} are the corresponding external radiative efficiency, which is the probability an excited CT respectively S_1 state leads to photon emission. In general, $ERE_{CT} << ERE_{S_1}$. Then the situation may occur that $qV_{OC,rad}$ is nearly independent of the CT properties ($J^0_{rad,CT} < J^0_{rad,S_1}$) but that non-radiative recombination of the CT state determines the V_{OC}. In our blends, this situation is suggested by the characteristic dependence of $V_{OC,rad}$ and V_{OC} on ΔE_{S_1-CT} (see **Figure 4**a). With decreasing ΔE_{S_1-CT} (increasing ICBA content) $V_{OC,rad}$ approaches a constant value, which implies that J^0_{rad,S_1} dominates over $J^0_{rad,CT}$ in Equation (5). On the other hand, there is a steady increase of V_{OC} with ICBA content through the entire composition range, suggesting that the V_{OC} remains dominated by the CT recombination properties where $\frac{J^0_{rad,CT}}{ERE_{CT}}$ decreases continuously with increasing E_{CT} in Equation (4).

To substantiate this conclusion, knowledge about the singlet state properties J^0_{rad,S_1} and ERE_{S_1} is needed. The ERE_{S_1} (i.e., the probability that an excited singlet state emits a photon to the outside), can be estimated through the measurements of the external photoluminescence quantum efficiency of the neat polymer. For 1F-PCPDTBT blended into polystyrene as an inert matrix, this yields a value of $(1.0 \pm 0.15) \times 10^{-3}$. On the other hand, J^0_{rad,S_1} can be gained from the deconvolution of the measured EQE_{PV} into the CT and S_1 components, which is however error prone due to the large overlap of the two components, especially for high ICBA content. Alternatively, we made use of the fact that (again assuming kinetic equilibrium between free charges, CT states and singlet excitons) the contributions of the two states to ELQY can be written as:

$$ELQY_{CT} = \frac{J^0_{rad,CT}}{J_{inj}} \exp\left(\frac{q\mu}{k_B T}\right) \quad (6)$$

$$ELQY_{S_1} = \frac{J^0_{rad,S_1}}{J_{inj}} \exp\left(\frac{q\mu}{k_B T}\right) \quad (7)$$

J_{inj} is the injection current which creates the chemical potential μ in the active layer. Here, it is reasonable to choose $\mu = qV_{OC}$ and $J_{inj} = J_{SC}$. Under these presumptions, $J^0_{rad,CT}$ and J^0_{rad,S_1} can be directly deduced from the experimental ELQY data, but we prefer to base the analysis on a physical model.

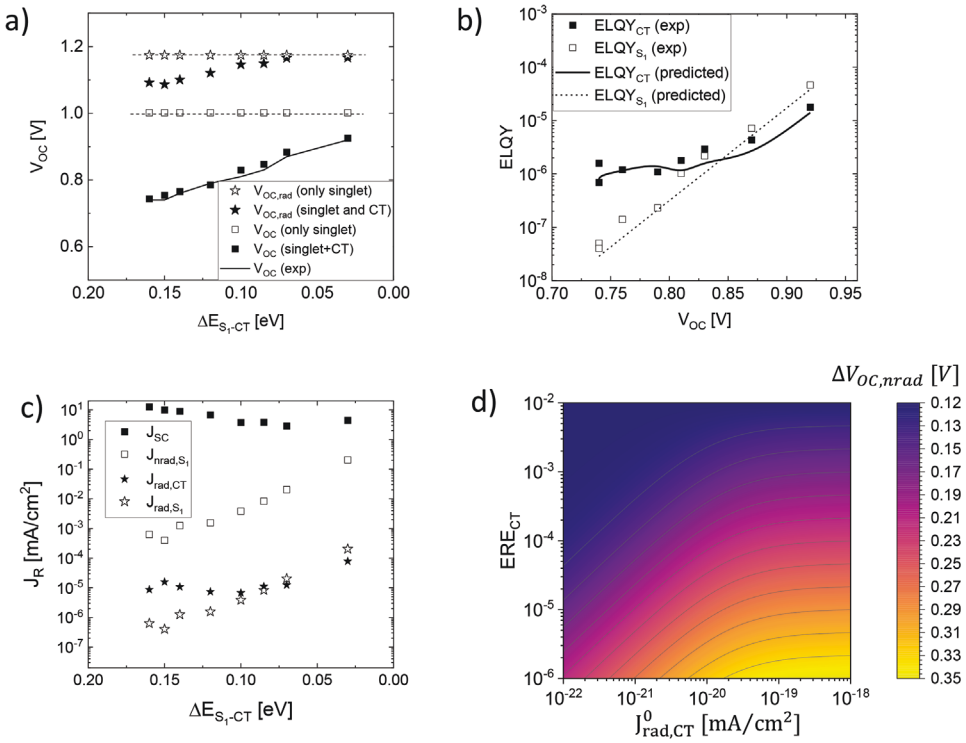

Figure 4. a) Dependency of $V_{OC,rad}$ and V_{OC} on ΔE_{S_1-CT}. Shown with full symbols are the predictions according to Equation (1) (with the measured J^0_{rad} and ELQY) while the open symbols show the prediction of Equations (4) and (5) if recombination proceeds entirely through the polymer S_1. The black line depicts the experimental results for the V_{OC}. b) $ELQY_{CT}$ and $ELQY_{S1}$ and the result of the fit according to Equations (6) and (7) with $J^0_{rad,S_1} = 4\times10^{-21}\times J_{SC}$ and $J^0_{rad,CT} = J^0_{rad} - J^0_{rad,S_1}$. c) The radiative and non-radiative recombination currents due to the singlet and CT population, compared to J_{SC}, plotted as function of the energy gap between singlet and CT-state (ΔE_{S_1-CT}). d) Heat map of $\Delta V_{OC,nrad}$ as function of $J^0_{rad,CT}$ and ERE_{CT} from Equation (8) using realistic singlet properties ($J^0_{rad,S_1} = 2\times10^{-20}$ mA cm^{-2}, $ERE_{S_1} = 10^{-2}$). The non-radiative V_{OC} loss for exclusive singlet recombination is 118 meV.

As shown in Figure 1b, the polymer absorption dominates the strongly absorbing spectral region which determines J_{SC} for all compositions. It is therefore plausible that $J^0_{rad,S_1} \propto J_{SC}$. Then, Equation (7) predicts that $ELQY_{S_1}$ increases strictly exponentially with V_{OC}, which is indeed the case (see the comparison of the open squares and the dashed line in Figure 4b). Now using $J^0_{rad,CT} = J^0_{rad} - J^0_{rad,S_1}$, the experimental $ELQY_{CT}$ can be reproduced over the entire composition range without any further assumptions (the solid line in Figure 4b). The corresponding values of $J^0_{rad,CT}$ and J^0_{rad,S_1} are compared to the experimental J^0_{rad} in Figure S4, Supporting Information. The analysis shows nicely that $J^0_{rad,CT}$ dominates J^0_{rad} for low ICBA concentration (low E_{CT}), but that it decreases rapidly because the onset of the CT absorption shifts to higher photon energies. As a consequence, $J^0_{rad,CT} < J^0_{rad,S_1}$ for high ICBA concentration and the singlet properties determine J^0_{rad}.

With J^0_{rad,S_1} and ERE_{S_1} at hand, we are now in a position to calculate $V_{OC,S_1} = k_B T/q \ln\left\{\frac{J_{SC}}{J^0_{rad,S_1}} ERE_{S_1}\right\}$ and $V_{OC,rad,S_1} = k_B T/q \ln\left\{\frac{J_{SC}}{J^0_{rad,S_1}}\right\}$ in the limit that all recombinations, radiative and non-radiative, proceeds through the singlet state of the low bandgap component. The result is plotted as function of $\Delta E_{S_1,CT}$ by open symbols in Figure 4a. Both properties change only little with $\Delta E_{S_1,CT}$, because J^0_{rad,S_1} is roughly proportional to J_{SC} and $ERE_{S_1} = \text{const}$. While the $V_{OC,rad}$ of the blend devices approaches this radiative singlet limit for high ICBA concentration, the V_{OC} always remains below the corresponding prediction for exclusive singlet recombination. This confirms our earlier conclusion that the singlet state dominates the radiative recombination currents for high x, through a higher J^0_{rad,S_1}, but it does not govern the total recombination current which determines V_{OC}. To substantiate this conclusion further, we calculated the current densities due to radiative singlet and CT decays from $J_{rad,S_1} = ELQY_{S_1} \times J_{SC}$. and $J_{rad,CT} = ELQY_{CT} \times J_{SC}$. The non-radiative singlet decay current density was estimated via $J_{nrad,S_1} = J_{rad,S_1} \frac{1-ERE_{S_1}}{ERE_{S_1}}$. These currents are compared to the J_{SC}, which we use as an approximation for the total recombination current as shown in Figure 4c (see Figure S5, Supporting Information, for the corresponding bar diagram). Both J_{rad,S_1} and J_{nrad,S_1} increase exponentially with decreasing ΔE_{S_1-CT}, due to a corresponding increase in V_{OC} and constant radiative efficiency. On the other hand, $J_{rad,CT}$ remains nearly constant. This is because the increase in V_{OC} (due to an increasing E_{CT}) is compensated by a corresponding decrease in $J^0_{rad,CT}$. Importantly, the total recombination current remains dominated by a non-radiative recombination process, which we assigned to the non-radiative CT decay, $J_{nrad,CT}$. The corresponding ERE_{CT} calculated from $J_{rad,CT}/(J_{rad,CT} + J_{nrad,CT})$ is shown in Figure S6, Supporting Information. ERE_{CT} increases exponentially with decreasing

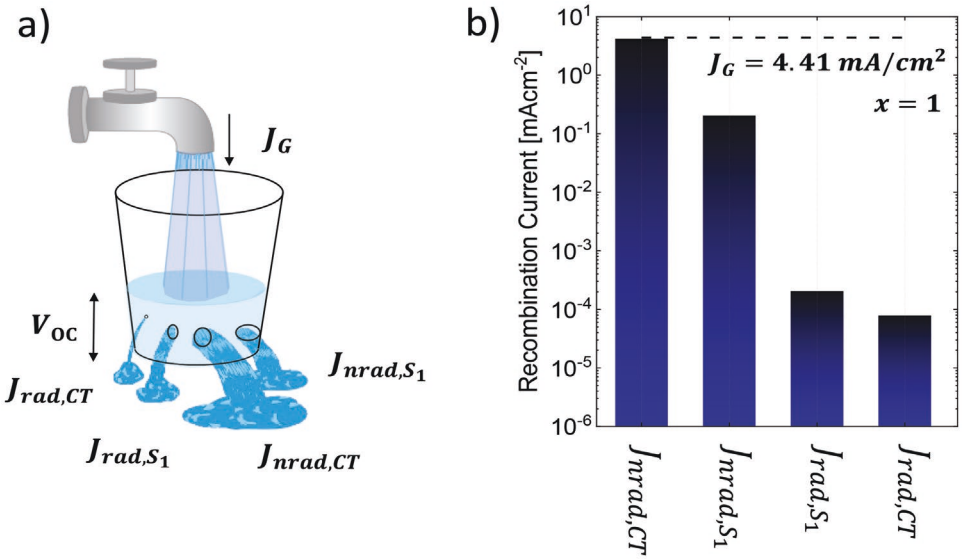

Figure 5. Free charge generation and recombination in the ICBA-rich blend ($x = 1$) illustrated by a a) bucket with holes and b) by a bar graph. While the radiative recombination is dominated by the decay of polymer singlet excitons, the non-radiative decay of CT excitons largely dominates the total recombination current and with that V_{OC}.

ΔE_{S_1-CT}, as expected from the energy gap law, with values ranging from 7×10^{-7} to 2×10^{-5} as being typical for CT states.

3. Discussion

By changing the composition of the acceptor phase, we tune the ternary blend from a situation, where the CT properties dictate both $V_{OC,rad}$ and the V_{OC}, to a mixed situation where the radiative properties are determined by the singlet state but the total recombination by the CT properties. We have illustrated the latter situation for the example of the ICBA-rich blend with $x = 1$ in **Figure 5**. Here, the generation of free charge is represented by a continuous water inflow into a bucket, while the holes in the bucket represent the outlet of the water from the bucket due to the different recombination currents. The height of the water is then representative of the V_{OC}.

The conditions and corresponding equations for CT-dominated and mixed situation are listed in **Table 1**. We have also added the prerequisites and equations for the singlet dominated case, which is however not realized in our blends, probably because of the highly non-radiative properties of the CT state. Recent work suggested that predominate singlet exciton recombination may become possible for fullerene and NFA-based systems with a low energy offset.[12,13,35]

Interestingly, neither the CT-dominated nor the mixed case depends on the emission efficiency of the singlet state, ERE_{S_1}. This contrasts the often-noted expectation that the V_{OC} generally benefits from a more emissive singlet exciton. Here, its intuitive to consider the non-radiative voltage loss. As outlined in the Supporting Information, $\Delta V_{OC,nrad}$ can be written as,

$$\Delta V_{OC,nrad} = V_{OC,rad} - V_{OC} = -k_B T \ln\left\{\frac{J^0_{rad,CT} + J^0_{rad,S_1}}{\frac{J^0_{rad,CT}}{ERE_{CT}} + \frac{J^0_{rad,S_1}}{ERE_{S_1}}}\right\} \quad (8)$$

In our blends, with decreasing ΔE_{S_1-CT}, the denominator becomes dominated by J^0_{rad,S_1} while the numerator remains governed by $\frac{J^0_{rad,CT}}{ERE_{CT}}$. Accordingly, the singlet exciton reduces the non-radiative voltage loss not because its more emissive, but because its strong absorption lowers the radiative V_{OC} limit. As such, $\Delta V_{OC,nrad}$ is nearly independent of the radiative efficiency of the S_1 state despite the fact that it is more emissive ($ERE_{S_1} > ERE_{CT}$). This is documented in Figure S7, Supporting

Table 1. Different scenarios for the contribution of the S_1 and the CT state to the radiative and total recombination currents and the corresponding equations for the open circuit voltage and the voltage loss. Also considered are the effect of increasing radiative efficiency, ERE_{S_1}, and increasing coupling strength between the singlet and CT excited states, t_{CT-S_1}.

Recombination	CT-dominated	Mixed case	S_1 dominated
Conditions	$J^0_{rad,CT} > J^0_{rad,S_1}$ $\frac{J^0_{rad,CT}}{ERE_{CT}} > \frac{J^0_{rad,S_1}}{ERE_{S_1}}$	$J^0_{rad,CT} < J^0_{rad,S_1}$ $\frac{J^0_{rad,CT}}{ERE_{CT}} > \frac{J^0_{rad,S_1}}{ERE_{S_1}}$	$J^0_{rad,CT} < J^0_{rad,S_1}$ $\frac{J^0_{rad,CT}}{ERE_{CT}} < \frac{J^0_{rad,S_1}}{ERE_{S_1}}$
$qV_{OC,rad} =$	$k_B T \ln\left\{\frac{J_R}{J^0_{rad,CT}}\right\}$	$k_B T \ln\left\{\frac{J_R}{J^0_{rad,S_1}}\right\}$	$k_B T \ln\left\{\frac{J_R}{J^0_{rad,S_1}}\right\}$
$qV_{OC} =$	$k_B T \ln\left\{\frac{J_R}{\frac{J^0_{rad,CT}}{ERE_{CT}}}\right\}$	$k_B T \ln\left\{\frac{J_R}{\frac{J^0_{rad,CT}}{ERE_{CT}}}\right\}$	$k_B T \ln\left\{\frac{J_R}{\frac{J^0_{rad,S_1}}{ERE_{S_1}}}\right\}$
$q\Delta V_{OC,nrad} =$	$-k_B T \ln\{ERE_{CT}\}$	$-k_B T \ln\left\{\frac{\frac{J^0_{rad,S_1}}{J^0_{rad,CT}}}{ERE_{CT}}\right\}$	$-k_B T \ln\{ERE_{S_1}\}$
increasing ERE_{S_1}	no effect	no effect	increases qV_{OC}, reduces $\Delta V_{OC,nrad}$
increasing t_{CT-S_1}	reduces $qV_{OC,rad}$ and $\Delta V_{OC,nrad}$, no effect on V_{OC}	no effect	no effect

Information, where we plot the measured $\Delta V_{OC,nrad}$ together with predictions from Equation (8) for $ERE_{S_1} = 10^{-2}$ and 10^{-5}, while all other parameters were taken from the above analysis. It is only if ERE_{CT} is strongly increased (or $J^0_{rad,CT}$ is largely reduced) that the $\Delta V_{OC,nrad}$ benefits from the singlet state occupation. This points to the importance of understanding and tuning the CT decay properties. To illustrate this conclusion, Figure 4d shows a heat map of $\Delta V_{OC,nrad}$ for realistic singlet properties ($J^0_{rad,S_1} = 2\times10^{-20}$ mA cm^{-2}, $ERE_{S_1} = 10^{-2}$),[9,10,36] while $J^0_{rad,CT}$ and ERE_{CT} are varied over four orders of magnitude. $\Delta V_{OC,nrad}$ becomes fully dominated by singlet exciton recombination with $\Delta V_{OC,nrad} = -k_B T \ln\{ERE_{S_1}\} = 118$ meV only for rather extreme CT state parameters ($J^0_{rad,CT} < 0.1\times J^0_{rad,S1}$, $ERE_{CT} > 10^{-3}$). We have recently shown that in the PM6:Y6 blend, the CT state is almost hidden under the much stronger singlet absorption. However, due to its very small radiative efficiency, recombination from the CT state was still fast and highly non-radiative, explaining the rather large $\Delta V_{OC,nrad}$ of 270 meV for this blend.

Let us finally consider the potential benefit of electronic coupling between the singlet and the CT states. In the limit of weak coupling, electronic coupling increases the oscillator strength of the CT state due to intensity borrowing from the singlet state, while it does not change its energy.[37,38] As a consequence, $J^0_{rad,CT}$ will generally increase with increasing coupling strength, t_{CT-S_1}, between the CT state and the singlet state, causing a concurrent raise of the radiative CT decay.[7] On the other hand, recent simulation work suggested that the non-radiative recombination rate is barely affected by t_{CT-S_1}.[12] As such, $ERE_{CT} \propto J^0_{rad,CT}$ and $\frac{J^0_{rad,CT}}{ERE_{CT}}$ is independent of t_{CT-S_1}. Under these prerequisites, V_{OC} does not depend on the electronic coupling t_{CT-S_1} in any of the situations discussed above. On the other hand, an increased electronic coupling will decrease $\Delta V_{OC,nrad}$ in the CT-dominated case, consistent with earlier work,[7,12] mainly because it increases $J^0_{rad,CT}$ and decreases $V_{OC,rad}$ while leaving V_{OC} unaffected.

Our work highlights the importance of reducing the non-radiative decay rate of the CT states, which we denote here as $k_{CT,nr}$. In the simplest case that this process proceeds though vibronic coupling to the electronic ground state, $k_{CT,nr}$ depends primarily on the CT energy though an energy gap law.[5] However, there are several other parameters determining $k_{CT,nr}$, such as the CT oscillator strength or the low and high frequency reorganization energies.[39,40] These properties depend strongly on the details of the chemical architecture of the molecules and their arrangement.[41,42] Another important factor is the degree of CT delocalization due to the aggregation of the donor and/or acceptor molecules. For the prototypical pentacene-C_{60} couple, computational work showed that $k_{CT,nr}$ increases strongly with the number of aggregated pentacene molecules at the heterojunction, and also depends on the relative orientation, in part due to a different CT state energy.[43] Notably, a change in the orientation of the pentacene molecules relative to the interface from the edge-on to the face-on decreased $k_{CT,nr}$ by up to a factor of ten. A substantial improvement of the V_{OC} in the face-on orientation has been demonstrated experimentally and attributed to reduced non-radiative losses.[44] This highlights the importance of tuning and optimizing molecular aggregation and orientation. Recent work highlighted the role of energetic disorder σ_{CT} on $k_{CT,nr}$.[40,45] It was predicted that reducing σ_{CT} can cause a substantial decrease of $k_{CT,nr}$, mainly by providing a smaller number of low energy CT states with high non-radiative decay rates. There are other means to increase the V_{OC} without the need to decrease the CT rate. As pointed out earlier, V_{OC} is dependent on the number density of CT states, N_{CT} through $eV_{OC} \propto \ln(N_{CT})$.[34] This may be achieved by dilution of the components as well as by reducing the degree of intermixing. State of the art NFAs exhibit a high tendency to form large and pure molecular aggregates in the BHJ film.[46] Finally, one may aim at entering the S_1 dominated recombination regime by decreasing ΔE_{S_1-CT} where V_{OC} and $\Delta V_{OC,nrad}$ become independent of the CT decay properties (see Table S1, Supporting Information). However, this approach often leads to a decrease of the J_{SC}, as also observed here.[9,19,47] A recent study gave promise that the S_1-dominated recombination regime may be entered without compromising the photocurrent generation efficiency.[12] Further research is needed to understand which specific properties renders these DA combinations so efficient despite a small energy offset.

4. Conclusion

We studied radiative and non-radiative recombination in a ternary blend of a well-aggregated low-bandgap polymer and a mixture of PCBM and ICBA. This allowed us to continuously tune the CT state energy while leaving the energy of the low energy polymer singlet exciton nearly unaffected. We find that for high ICBA concentrations the latter dominates the radiative properties of the blend, while the former determines the non-radiative processes and, with this, the V_{OC}. In this regime, the non-radiative loss decreases with increasing ICBA content because a blue-shifted and more radiative CT state raises V_{OC} while at the same time the strongly absorbing S_1 sets an upper limit to the $V_{OC,rad}$. Our data shows that a strong singlet exciton contribution in the absorption and emission of D:A blends does not necessary imply that the V_{OC} benefits from the repopulation of the S_1, even in the case of a small S_1-CT offset. Considering only the non-radiative voltage loss to evaluate V_{OC} limiting processes is insufficient. Instead, a careful analysis of all contributions (radiative and non-radiative) to the total recombination is crucial in the development and optimization of new materials and their blends for organic solar cells.

5. Experimental Section

Sample Fabrication: The solar cell devices were fabricated on structured ITO-coated glass slides (Optrex) pre-cleaned in acetone, detergent, DI-water, and isopropanol, and dried with a nitrogen gun. The pre-cleaned ITO substrate was plasma-cleaned and a 50–60 nm layer of PEDOT:PSS (Clevios AI 4083) was spin cast on top. After transferring the substrates into nitrogen filled glove-box the active layer was spin cast from solutions of a constant polymer weight fraction and variable PCBM:ICBA ratio: $c_{1F\text{-}PCPDTBT}$:c_{PC70BM}:c_{ICBA} = 1: 3(1 − *x*): 3*x*.

1F-PCPDTBT (M_w = 55789 g mol^{-1}, PDI = 1.46) was synthesized as described in Albrecht et al.[18] $PC_{70}BM$ (99%, Solenne) and ICBA (99%, Solenne) were used as received. Dichlorobenzene was used as solvent and all samples were prepared with 1 vol% DIO as processing agent. Finally, 20 nm Ca and 100 nm Al were thermally evaporated with a base

pressure below 10^{-6} mbar trough shadow masks to define the active area to be 16 mm^2. Such a small area was used to realize a small RC-constant of the device. Due to the high boiling point of DIO, all devices processed with DIO were dried in vacuum at room-temperature for at least 2 h prior the evaporation of Ca and Al, since residual DIO functions as a hole trap. All samples were encapsulated with two component epoxy resin and a glass lid prior to air exposure.

Grazing-Incidence Wide-Angle X-Ray Scattering and Resonant Soft X-Ray Scattering: GIWAXS was conducted at beamline 7.3.3 at the Advanced Light Source (ALS), Lawrence Berkeley National Laboratory using 10 keV photons at an incident angle of 0.2°. Samples were cast onto silicon substrates coated with PSS to replicate device morphology. RSoXS measurements were carried out at beamline 11.0.1.2 at the ALS. X-ray energy was chosen to maximize phase contrast between components and limit background signal from X-ray fluorescence. Samples were floated from silicon substrates coated in water-soluble PSS in deionized water onto silicon nitride windows for RSoXS measurements.

Solar Cell Characteristics: The solar cell characteristics were measured with an Oriel class A simulator calibrated to 100 mW cm^{-2}, and the samples were temperature controlled to 20 °C during measurement. The calibration of the sun simulator was done with a KG3 filtered silicon reference cell calibrated at Fraunhofer ISE.

Electroluminescence Measurements: In addition to an Andor Solis 803 System consisting of mirrors and filters, a Si-Detector (90 averages with 1s integration time) and one grid for a center wavelength (CWL) of 800 nm and an InGaAs-Detector (1 average with 90s integration time) with another grid for CWL equaling 1100 and 1400 nm, were used. The measurements were done close to V_{OC}-condition.

Photovoltaic External Quantum Efficiency Measurements: The light source was a Philips halogen lamp with 300 W whose light was chopped with 87 Hz and gets monochromated with an Oriel 260 Monochromator. Due to high order effects during the refraction at the grid edge filter was used for 650 and 780 nm, respectively. The spectra were calibrated with a Si-Diode (Newport UV 818) until 800 nm but above with an InGaAs-Diode (Newport IR 918) while the signal was read out by an analog Lock-In Amplifier (EG&G 5302).

Photoluminescence Quantum Yield: Photoluminescence quantum yield measurements were performed on films of neat 1F-PCPDTBT and a 1:1 w/w blend of 1F-PCPDTBT with polystyrene (M_w = 35 000 g mol^{-1}). The samples were encapsulated carefully along the edges making sure that the central illuminated area was free of the encapsulation glue. Additionally, the edges of the samples were covered with black tape to avoid waveguiding through the sides. The measurements were performed inside an integrating sphere (Hamamatsu Photonics K.K. A10094) under steady state illumination of a 520 nm continuous wave laser (InsaneWare). The intensity of the laser was adjusted to a 1 sun equivalent using a calibrated Si photodiode. The photoluminescence signal at the output of the integrating sphere was detected using an Andor Shamrock SR-303i-B spectrograph equipped with a DU420A-BR-DD Si detector (for CWL of 800 nm) and a DU491A-1.7 InGaAs detector (for CWL of 1100 and 1400 nm).

Supporting Information

Supporting Information is available from the Wiley Online Library or from the author.

Acknowledgements

This work has been funded by the German Science Foundation DFG) Project Nos. 256605806 and 460766640. Nanostructure X-ray characterization was supported by the US National Science Foundation Grant #1905790 and used resources of the Advanced Light Source, which is a DOE Office of Science User Facility under Contract No. DE-AC02-05CH11231. The authors also thank Lorena Perdigon Toro and Manasi Pranav for their feedback on the manuscript.

Open access funding enabled and organized by Projekt DEAL.

Conflict of Interest

The authors declare no conflict of interest.

Data Availability Statement

The data that support the findings of this study are available in the supplementary material of this article.

Keywords

external quantum efficiency, organic photovoltaics, ternary blends, voltage losses

Received: February 24, 2022
Revised: May 12, 2022
Published online: June 28, 2022

[1] S. E. Shaheen, C. J. Brabec, N. S. Sariciftci, F. Padinger, T. Fromherz, J. C. Hummelen, *Appl. Phys. Lett.* **2001**, *78*, 841.
[2] Y. Cui, Y. Xu, H. Yao, P. Bi, L. Hong, J. Zhang, Y. Zu, T. Zhang, J. Qin, J. Ren, Z. Chen, C. He, X. Hao, Z. Wei, J. Hou, *Adv. Mater.* **2021**, *33*, 41.
[3] Z. Zheng, J. Wang, P. Bi, J. Ren, Y. Wang, Y. Yang, X. Liu, S. Zhang, J. Hou, *Joule* **2022**, *6*, 171.
[4] A. Armin, W. Li, O. J. Sandberg, Z. Xiao, L. Ding, J. Nelson, D. Neher, K. Vandewal, S. Shoaee, T. Wang, H. Ade, T. Heumüller, C. Brabec, P. Meredith, *Adv. Energy Mater.* **2021**, *11*, 2003570.
[5] J. Benduhn, K. Tvingstedt, F. Piersimoni, S. Ullbrich, Y. Fan, M. Tropiano, K. A. McGarry, O. Zeika, M. K. Riede, C. J. Douglas, S. Barlow, S. R. Marder, D. Neher, D. Spoltore, K. Vandewal, *Nat. Energy* **2017**, *2*, 6.
[6] S. Ullbrich, J. Benduhn, X. Jia, V. C. Nikolis, K. Tvingstedt, F. Piersimoni, S. Roland, Y. Liu, J. Wu, A. Fischer, D. Neher, S. Reineke, D. Spoltore, K. Vandewal, *Nat. Mater.* **2019**, *18*, 459.
[7] F. D. Eisner, M. Azzouzi, Z. Fei, X. Hou, T. D. Anthopoulos, T. J. S. Dennis, M. Heeney, J. Nelson, *J. Am. Chem. Soc.* **2019**, *141*, 6362.
[8] D. Qian, Z. Zheng, H. Yao, W. Tress, T. R. Hopper, S. Chen, S. Li, J. Liu, S. Chen, J. Zhang, X.-K. Liu, B. Gao, L. Ouyang, Y. Jin, G. Pozina, I. A. Buyanova, W. M. Chen, O. Inganäs, V. Coropceanu, J.-L. Bredas, H. Yan, J. Hou, F. Zhang, A. A. Bakulin, F. Gao, *Nat. Mater.* **2018**, *17*, 703.
[9] A. Classen, C. L. Chochos, L. Lüer, V. G. Gregoriou, J. Wortmann, A. Osvet, K. Forberich, I. McCulloch, T. Heumüller, C. J. Brabec, *Nat. Energy* **2020**, *5*, 711.
[10] L. Perdigón-Toro, L. Q. Phuong, S. Zeiske, K. Vandewal, A. Armin, S. Shoaee, D. Neher, *ACS Energy Lett.* **2021**, *6*, 557.
[11] O. J. Sandberg, A. Armin, *J. Phys. Chem. C* **2021**, *125*, 15590.
[12] X.-K. Chen, D. Qian, Y. Wang, T. Kirchartz, W. Tress, H. Yao, J. Yuan, M. Hülsbeck, M. Zhang, Y. Zou, Y. Sun, Y. Li, J. Hou, O. Inganäs, V. Coropceanu, J.-L. Bredas, F. Gao, *Nat. Energy* **2021**, *6*, 8.
[13] Y. Dong, H. Cha, H. L. Bristow, J. Lee, A. Kumar, P. S. Tuladhar, I. McCulloch, A. A. Bakulin, J. R. Durrant, *J. Am. Chem. Soc.* **2021**, *143*, 20.
[14] R. A. Street, D. Davies, P. P. Khlyabich, B. Burkhart, B. C. Thompson, *J. Am. Chem. Soc.* **2013**, *135*, 986.
[15] S. Kouijzer, W. Li, M. Wienk, R. Janssen, *J. Photonics Energy* **2014**, *5*, 057203.
[16] A. Sperlich, M. Auth, V. Dyakonov, *Isr. J. Chem.* **2021**, *61*, 1.
[17] Y. Zhang, J. Zou, C.-C. Cheuh, H.-L. Yip, A. K. Y. Jen, *Macromolecules* **2012**, *45*, 13.

[18] S. Albrecht, S. Janietz, W. Schindler, J. Frisch, J. Kurpiers, J. Kniepert, S. Inal, P. Pingel, K. Fostiropoulos, N. Koch, D. Neher, *J. Am. Chem. Soc.* **2012**, *134*, 36.
[19] J. Kurpiers, T. Ferron, S. Roland, M. Jakoby, T. Thiede, F. Jaiser, S. Albrecht, S. Janietz, B. A. Collins, I. A. Howard, D. Neher, *Nat. Commun.* **2018**, *9*, 2038.
[20] L. Ye, H. Hu, M. Ghasemi, T. Wang, B. A. Collins, J.-H. Kim, K. Jiang, J. H. Carpenter, H. Li, Z. Li, T. McAfee, J. Zhao, X. Chen, J. L. Y. Lai, T. Ma, J.-L. Bredas, H. Yan, H. Ade, *Nat. Mater.* **2018**, *17*, 253.
[21] J. Peet, J. Y. Kim, N. E. Coates, W. L. Ma, D. Moses, A. J. Heeger, G. C. Bazan, *Nat. Mater.* **2007**, *6*, 497.
[22] J. K. Lee, W. L. Ma, C. J. Brabec, J. Yuen, J. S. Moon, J. Y. Kim, K. Lee, G. C. Bazan, A. J. Heeger, *J. Am. Chem. Soc.* **2008**, *130*, 11.
[23] F. C. Jamieson, E. B. Domingo, T. McCarthy-Ward, M. Heeney, N. Stingelin, J. R. Durrant, *Chem. Sci.* **2012**, *3*, 485.
[24] S. Shoaee, T. M. Clarke, C. Huang, S. Barlow, S. R. Marder, M. Heeney, I. McCulloch, J. R. Durrant, *J. Am. Chem. Soc.* **2010**, *132*, 12919.
[25] S. Roland, L. Yan, Q. Zhang, X. Jiao, A. Hunt, M. Ghasemi, H. Ade, W. You, D. Neher, *J. Phys. Chem. C* **2017**, *121*, 10305.
[26] U. Rau, *Phys. Rev. B* **2007**, *76*, 8.
[27] A. Armin, N. Zarrabi, O. J. Sandberg, C. Kaiser, S. Zeiske, W. Li, P. Meredith, *Adv. Energy Mater.* **2020**, *10*, 2001828.
[28] M. List, T. Sarkar, P. Perkhun, J. Ackermann, C. Luo, U. Würfel, *Nat. Commun.* **2018**, *9*, 3631.
[29] S. A. Mollinger, K. Vandewal, A. Salleo, *Adv. Energy Mater.* **2015**, *5*, 1501335.
[30] N. Felekidis, E. Wang, M. Kemerink, *Energy Environ. Sci.* **2016**, *9*, 257.
[31] S. Shoaee, S. Subramaniyan, H. Xin, C. Keiderling, P. S. Tuladhar, F. Jamieson, S. A. Jenekhe, J. R. Durrant, *Adv. Funct. Mater.* **2013**, *23*, 3286.
[32] F.-J. Kahle, A. Rudnick, H. Bässler, A. Köhler, *Mater. Horiz.* **2018**, *5*, 837.
[33] C. Göhler, M. Saladina, Y. Wang, D. Spoltore, J. Benduhn, K. Leo, C. Deibel, *Phys. Rev. Appl.* **2021**, *15*, 6.
[34] T. M. Burke, S. Sweetnam, K. Vandewal, M. D. McGehee, *Adv. Energy Mater.* **2015**, *5*, 1500123.
[35] R. Shivhare, G. J. Moore, A. Hofacker, S. Hutsch, Y. Zhong, M. Hambsch, T. Erdmann, A. Kiriy, S. C. B. Mannsfeld, F. Ortmann, N. Banerji, *Adv. Mater.* **2022**, *34*, 2101784.
[36] Y. Firdaus, V. M. Le Corre, S. Karuthedath, W. Liu, A. Markina, W. Huang, S. Chattopadhyay, M. M. Nahid, M. I. Nugraha, Y. Lin, A. Seitkhan, A. Basu, W. Zhang, I. McCulloch, H. Ade, J. Labram, F. Laquai, D. Andrienko, L. J. A. Koster, T. D. Anthopoulos, *Nat. Commun.* **2020**, *11*, 5220.
[37] K. Vandewal, K. Tvingstedt, O. Inganäs, *Phys. Rev. B* **2012**, *86*, 3.
[38] X.-K. Chen, V. Coropceanu, J.-L. Brédas, *Nat. Commun.* **2018**, *9*, 5295.
[39] M. Azzouzi, J. Yan, T. Kirchartz, K. Liu, J. Wang, H. Wu, J. Nelson, *Phys. Rev. X* **2018**, *8*, 3.
[40] T. Wang, V. Coropceanu, J.-L. Brédas, *Chem. Mater.* **2019**, *31*, 16.
[41] K. R. Graham, C. Cabanetos, J. P. Jahnke, M. N. Idso, A. El Labban, G. O. N. Ndjawa, T. Heumueller, K. Vandewal, A. Salleo, B. F. Chmelka, A. Amassian, P. M. Beaujuge, M. D. McGehee, *J. Am. Chem. Soc.* **2014**, *136*, 27.
[42] K. Vandewal, J. Benduhn, K. S. Schellhammer, T. Vangerven, J. E. Rückert, F. Piersimoni, R. Scholz, O. Zeika, Y. Fan, S. Barlow, D. Neher, S. R. Marder, J. Manca, D. Spoltore, G. Cuniberti, F. Ortmann, *J. Am. Chem. Soc.* **2017**, *139*, 1699.
[43] X.-K. Chen, M. K. Ravva, H. Li, S. M. Ryno, J.-L. Brédas, *Adv. Energy Mater.* **2016**, *6*, 24.
[44] N. A. Ran, S. Roland, J. A. Love, V. Savikhin, C. J. Takacs, Y.-T. Fu, H. Li, V. Coropceanu, X. Liu, J.-L. Brédas, G. C. Bazan, M. F. Toney, D. Neher, T.-Q. Nguyen, *Nat. Commun.* **2017**, *8*, 79.
[45] Z. Zheng, N. R. Tummala, T. Wang, V. Coropceanu, J.-L. Brédas, *Adv. Energy Mater.* **2019**, *9*, 14.
[46] K. Jiang, Q. Wei, J. Y. L. Lai, Z. Peng, H. K. Kim, J. Yuan, L. Ye, H. Ade, Y. Zou, H. Yan, *Joule* **2019**, *3*, 3020.
[47] S. Karuthedath, J. Gorenflot, Y. Firdaus, N. Chaturvedi, C. S. De Castro, G. T. Harrison, J. I. Khan, A. Markina, A. H. Balawi, T. A. D. Peña, *Nat. Mater.* **2021**, *20*, 378.